

A Scalable Dealloying Technique To Create Thermally Stable Plasmonic Nickel Selective Solar Absorbers

Meijie Chen,^{†,‡,§} Jyotirmoy Mandal,[†] Qin Ye,[†] Aijun Li,[†] Qian Cheng,[†] Tianyao Gong,[†] Tianwei Jin,[†] Yurong He,[‡] Nanfang Yu,[†] and Yuan Yang^{*,†,§}

[†]Department of Applied Physics and Applied Mathematics, Columbia University, New York, New York 10027, United States

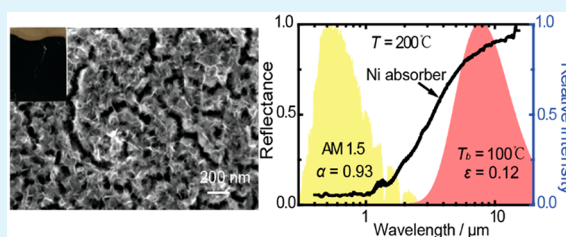
[‡]School of Energy Science & Engineering, Harbin Institute of Technology, Harbin 150001, P. R. China

[§]School of Energy Science & Engineering, Central South University, Changsha 410083, P. R. China

Supporting Information

ABSTRACT: The single-element-based selective solar absorber (SSA) is attractive as it does not suffer from mismatched thermal expansion and consequent performance degradation in composite selective solar absorbers. In this report, a simple and scalable dealloying method is demonstrated for fabricating SSAs with high durability. The porous nickel SSAs prepared through this technique not only exhibit an applicable solar absorptance/thermal emittance (0.93/0.12 or 0.88/0.08) without the aid of antireflection coatings but also show an excellent thermal stability up to 200 °C in air over prolonged periods. Furthermore, the dealloying technique shows great tunable performance for the selective absorption of metal absorber, which can be used to fabricate the porous metallic structures for various working conditions.

KEYWORDS: nickel, solar selective absorber, dealloying, nanoporous, plasmonic



1. INTRODUCTION

A sustainable future urgently requires the use of clean and sustainable energy sources. Sunlight, which is one such source, is also green, abundant, and widespread. Efficient methods to convert solar energy into other forms are highly desired, such as photovoltaic,¹ photochemical,² and solar-to-thermal conversion.³ Solar-to-thermal conversion is highly convenient, as the thermal energy can be directly used, stored, or further converted into electricity.^{4,5} In solar–thermal systems, the solar selective absorber (SSA) is a key component as it effectively absorbs the solar energy and converts it to thermal energy.⁶ On the other hand, some smart solar absorbers or emitters were also designed for local temperature control.^{7,8}

An efficient solar selective absorber should have high absorptance in the solar spectrum spanning from 0.3 to 2.5 μm. Meanwhile, its spectral emittance at wavelengths corresponding to the blackbody spectrum at working temperature (e.g., 2.5–30 μm at 100 °C) should be as low as possible to minimize radiative loss. The overall performance of the SSA can be characterized by the solar thermal conversion efficiency η_s , which is determined by its operating temperature T , solar absorptance $\bar{\alpha}$, and thermal emittance $\bar{\epsilon}$.⁹ The solar thermal conversion efficiency η_s means the percentage of sunlight that can be converted to useful thermal energy by the selective absorber.¹⁰ It is the net flux of heat flow (absorbed sunlight subtracting thermal radiation) divided by all incident sunlight on a given area.

$$\eta_s = \bar{\alpha} - \frac{\bar{\epsilon} I_B(T)}{C I_s} \quad (1)$$

$$\bar{\alpha} = \frac{\int \alpha(\lambda) I_s(\lambda) d\lambda}{\int I_s(\lambda) d\lambda} \quad (2)$$

$$\bar{\epsilon} = \frac{\int \epsilon(\lambda) I_B(\lambda, T) d\lambda}{\int I_B(\lambda, T) d\lambda} \quad (3)$$

where λ is the wavelength, I_s is the solar intensity, I_B is the blackbody radiation at working temperature T , C is the solar concentration factor, and α and ϵ are the spectral absorptance and thermal emittance, and both can be expressed as $1 - R$ for opaque metallic SSAs, where R is the reflectance. An ideal SSA should have $\alpha = 1$ in the solar wavelengths and $\epsilon = 0$ in the thermal wavelengths. Based on the working temperature, currently selective absorbers can be divided into low temperature (<100 °C), mid-temperature (100–400 °C), and high temperature (>400 °C).¹¹ Regardless of the working temperature, $\bar{\alpha} \geq 0.8$ and $\bar{\epsilon} \leq 0.2$ are required for practical applications. Various approaches have been applied to the SSA design in recent decades, such as intrinsic absorbers, semiconductor–metal tandems, multilayer absorbers, metal–dielectric composite coatings, and surface texturing.^{12–14} The

Received: June 5, 2019

Accepted: August 16, 2019

Published: August 16, 2019

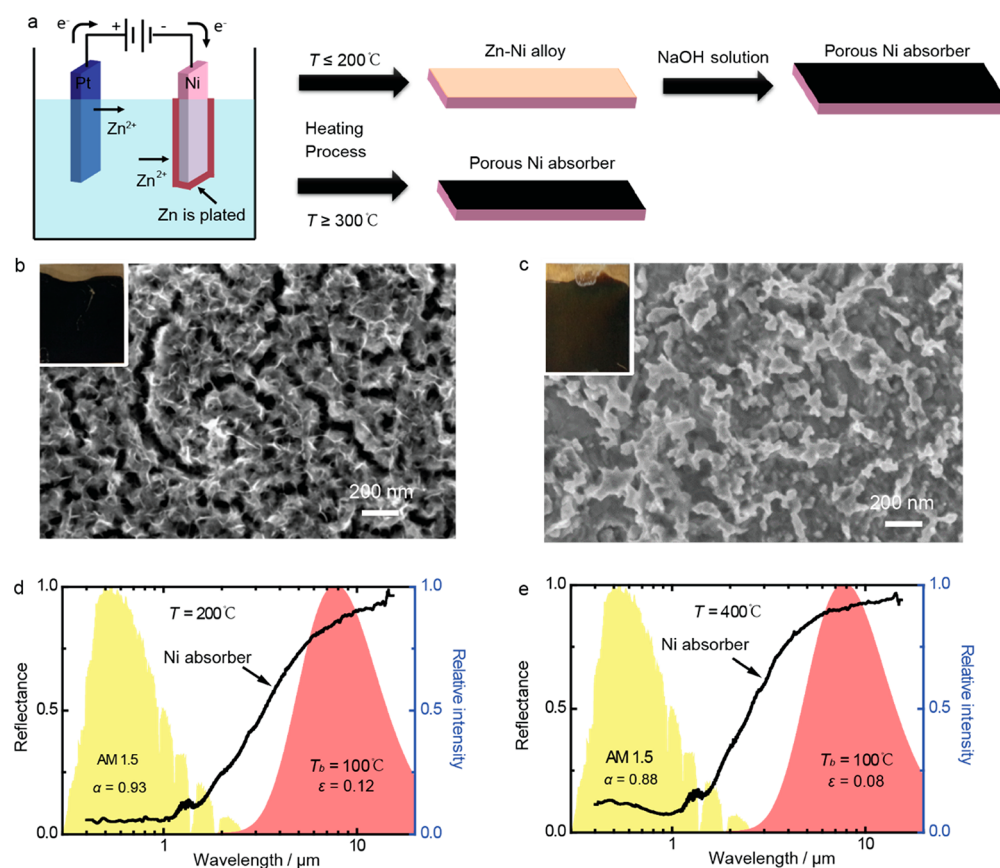


Figure 1. Preparation of single-element Ni SSAs. (a) Schematic illustration of the fabrication process for Ni SSAs. When the heating temperature is low (≤ 200 °C), chemical etching process is used for dealloying. On the other hand, vapor-phase dealloying is applied for the high heating temperature (≥ 300 °C). (b, c) SEM images of the nanoporous Ni absorber by (b) chemical etching dealloying method and (c) vapor-phase dealloying method. Insets are the corresponding optical images of the Ni absorbers. (d, e) Spectral reflectance of (d) a porous Ni SSA ($\bar{\alpha} = 0.93$, $\bar{\epsilon} = 0.12$) based on the chemical etching dealloying method and (e) a porous Ni SSA ($\bar{\alpha} = 0.88$, $\bar{\epsilon} = 0.08$) based on the vapor-phase dealloying method. Normalized spectral intensities of the AM 1.5 solar spectrum and a blackbody at 100 °C are also shown.

selectivity of intrinsic absorbers is an intrinsic property of the materials, which is structurally more stable but optically less effective than multilayer stacks.¹⁵ The other types all rely on structure to achieve the selective optical properties. For instance, metal–dielectric composite coatings are reflective in the thermal IR region, while they are strongly absorbing in the solar region because of interband transitions in the metal and plasmon resonances.^{16–19}

One significant challenge in such multicomponent selective absorber is that the mismatch in thermal expansion coefficient of metal and ceramic will cause fatigue and delamination in accumulated thermal cycles.²⁰ To address this challenge, single-element-based nanostructured metal SSAs such as metal tungsten array,^{21,22} tantalum array,²³ and nanostructure gold²⁴ have been proposed. However, the fabrication processes (such as reactive ion etching,²⁵ vapor deposition,²⁶ and atomic layer deposition²⁷) are usually complex and of high cost due to the micro- and nanopatterning of surfaces.²⁸ Moreover, the stability of nanostructures in the practical applications is needed to improve since the surface of the microstructure must be protected from damage caused by surface contact or abrasion.¹¹ Therefore, producing SSAs with long-term durability based on a single abundant element through a simple process is required. Here we develop a scalable method by combining electrodeposition, annealing, and dealloying to create nanoporous metal SSAs with attractive $\bar{\alpha}/\bar{\epsilon}$ (0.93/0.12

or 0.88/0.08) without the aid of antireflection coating. Because of the high thermal/chemical stability of Ni and the lack of large thermal strain induced by mismatched thermal expansion, the absorber also shows excellent thermal stability up to 200 °C in air for 96 h. Furthermore, this dealloying technique is a great candidate to tune the selective absorption performance of single-element porous metal absorber at different working conditions.

2. RESULTS AND DISCUSSION

Compared to the conventional dealloying method, the major challenge here is to form a thin layer of nanoporous Ni only at the Ni film surface. To solve this problem, a thin layer of Zn (e.g., ~ 300 nm) is first deposited onto a Ni substrate by electroplating. Then the sample is annealed at a relative low temperature (≤ 200 °C) so that Zn forms alloy with Ni (Figure 1a). Finally, Zn is removed by either chemical etching in the NaOH solution or vapor-phase dealloying at high temperature (≥ 300 °C) (Figure 1a). Further details are presented in the section S1 of the Supporting Information. As Zn has significantly higher vapor pressure than Ni at elevated temperature (e.g., 11 Pa vs 3×10^{-21} Pa at 400 °C, Figure S1b), Zn can be selectively removed by optimizing the processing temperature and pressure. Both approaches result in nanoporous Ni sponge, as demonstrated by SEM in Figure 1b,c. The porous Ni after dealloying processes appears black

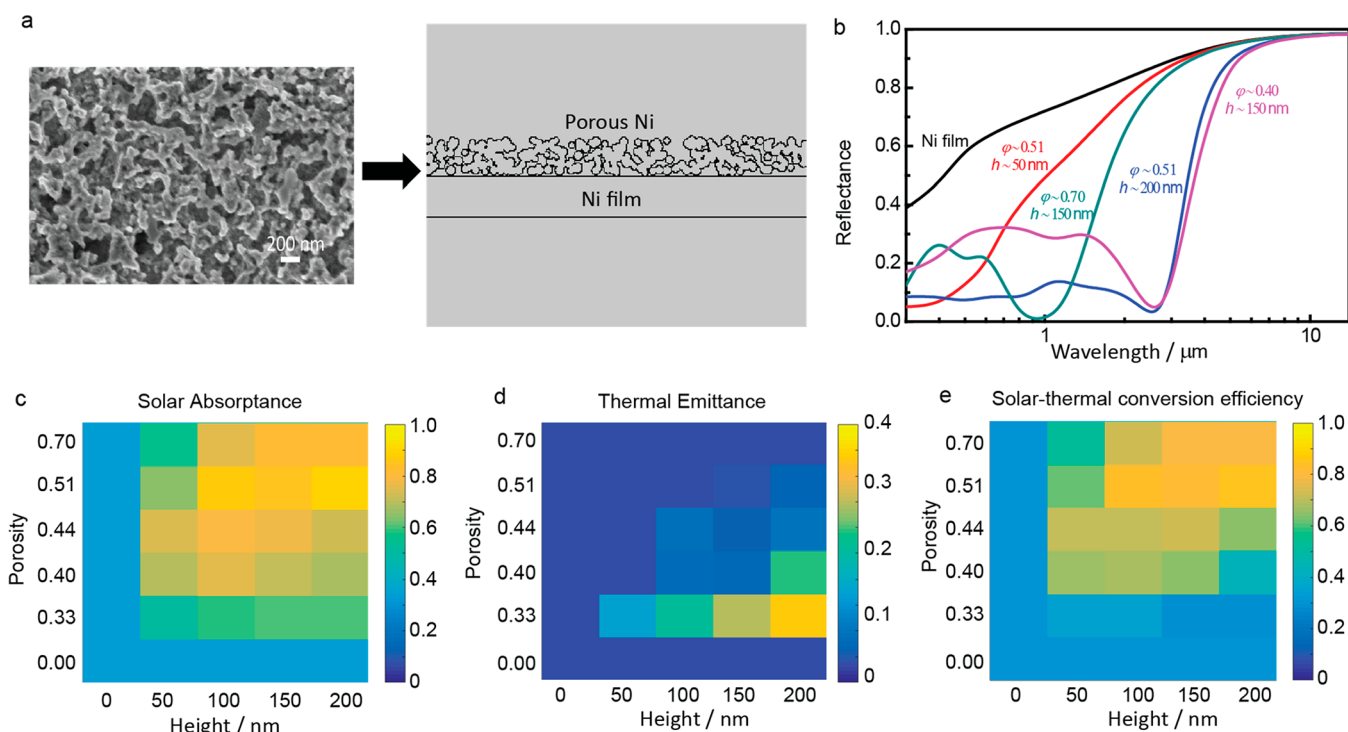


Figure 2. Simulation results of the Ni porous SSA. (a) Schematic of the simulated Ni porous SSA. The SEM image left shows the porous structure consisting of Ni particles. (b) Simulated spectra showing the effect of the height and the porosity of the porous layer. Panels c–e show (c) solar absorptance $\bar{\alpha}$, (d) thermal emittance $\bar{\epsilon}$, and (e) solar thermal conversion efficiency η_s at the normal incidence for different heights and porosities of the porous layer.

because of its plasmonic nanostructures, which strongly traps and absorbs sunlight and leads to a high solar absorptance (Figure 1d,e). Integrated sphere-based reflectance measurements reveal that the porous Ni selective absorber has an excellent optical selectivity ($\bar{\alpha} = 0.93$, $\bar{\epsilon} = 0.12$ for the chemical etching dealloying process in Figure 1b and $\bar{\alpha} = 0.88$, $\bar{\epsilon} = 0.08$ for the vapor-phase dealloying process in Figure 1d). Compared with other multicomponent nickel selective absorber using the solution-chemistry method to form nickel pigmented aluminum oxide ($\bar{\alpha}/\bar{\epsilon} = 0.83/0.03$,²⁹ $0.85/0.03$,³⁰ and $0.91\text{--}0.97/0.11\text{--}0.23$ ³¹), our work has similar solar selective absorption performance without using Al_2O_3 ($\bar{\alpha}/\bar{\epsilon} = 0.93/0.12$ for the chemical etching dealloying process and $\bar{\alpha}/\bar{\epsilon} = 0.88/0.08$ for the vapor-phase dealloying process). The removal of Al_2O_3 can potentially reduce thermal strain inside. Moreover, the stability and durability of the multicomponent nickel selective absorber should be further studied for the practical application.^{29,31} On the other hand, compared with previous works using reactive ion etching or atomic layer deposition to form single-element textured nickel metals ($\bar{\alpha} = 0.75$, $\bar{\epsilon} = 0.14$),²⁸ the large-scale nanofabrication process developed here is particularly cost-effective and robust, especially with only low-cost metals involved. During the vapor-phase dealloying step, a condensation unit can also be added to recycle the evaporated Zn to form the Ni–Zn alloy,³² that the reagent can be reused, leading to a low-cost and high-throughput fabrication process.

To understand how the nanoparticle morphology affects the selective absorption, the finite element method (FEM) was used to simulate the spectral absorptance of the Ni porous SSA; more simulation details can be found in section S2 of the Supporting Information. As shown in Figure 2a and Figure S2, the bottom Ni film served as an optically thick slab, on which

small Ni particles were randomly arranged to form the nanoporous Ni sponge. The diameters of the Ni particles varied from 10 to 30 nm randomly based on the smallest roughness since large irregular particles can be stacked by multi-small particles. The density of the Ni particles and thickness of the porous layer were tuned to investigate the effect of the porosity and height on reflectance spectra at normal incidence.

As shown in Figure 2b–e, as the height of the porous layer increases from 0 to 200 nm, both solar absorptance $\bar{\alpha}$ and thermal emittance $\bar{\epsilon}$ rise. In the solar spectra, it can be found that all porous structures lead to a stronger absorptance than that of the bulk Ni film due to the enhanced local surface plasmon resonance in the cavity of the porous structure. The absorption region becomes broader with an increasing porous layer height, which is attributed to the enhanced light–matter interaction among the cavities or particles at larger height. For example, at porosity $\phi = 0.51$, when h increases from 50 to 200 nm, $\bar{\alpha}$ changes from 0.65 to 0.91. On the other hand, at the mid-infrared region, the porous structure has a similar emittance with the bulk Ni film since the incident wavelength is much greater than feature length of the porous layer (Figure 2b).

A broader absorption region can also be seen with increasing the number of the Ni particles or decreasing the porosity while the absorption intensity decreases (Figure 2b). Moreover, increasing the porosity ϕ leads to an initial increase of solar absorptance $\bar{\alpha}$ and thermal emittance $\bar{\epsilon}$ followed by a descent (Figure 2c,d). For example, at the height of 150 nm, when the porosity ϕ increases from 0 to 0.7, $\bar{\alpha}$ increases from 0.33 to 0.86 due to the enhanced surface plasmon resonance of the Ni particles at the solar spectrum and then decreases to 0.82 since the number of the absorbing metal Ni nanoparticle decreases

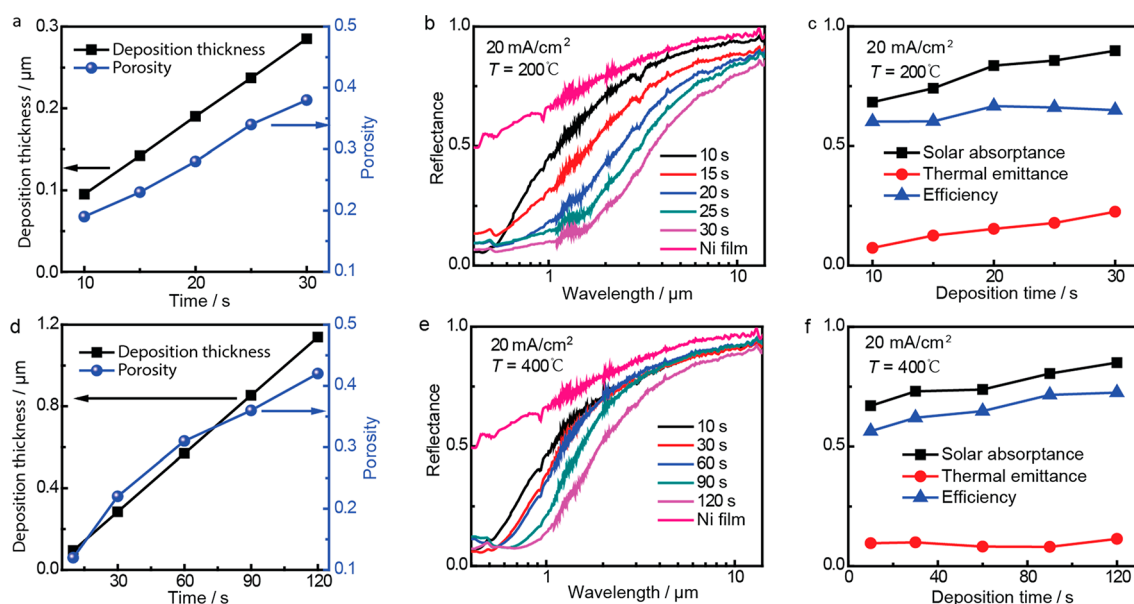


Figure 3. Dependence of geometry and optical performance of Ni absorbers on deposition time. (a–c) Chemical etching dealloying: (a) electrodeposition thickness and surface porosity of the Ni absorber, (b) spectral reflectance, and (c) $\bar{\alpha}$, $\bar{\varepsilon}$, and η_s . (d–f) Vapor-phase dealloying: (d) electrodeposition thickness and surface porosity of the Ni absorber, (e) spectral reflectance, (f) $\bar{\alpha}$, $\bar{\varepsilon}$, and η_s . When the heating temperature is 200 °C, the NaOH solution is used in the chemical etching dealloying process. For the heating temperature of 400 °C, the vapor-phase dealloying process is applied.

and the medium becomes less absorptive. $\bar{\varepsilon}$ increases from 0.03 to 0.28 due to plasmon resonances. Nonporous or solid nickel is a good reflector and poor emitter like typical metals, but in porous Ni, the Ni particles are small (10–30 nm) relative to the thermal wavelengths and plasmonic, so compared to bulk Ni, the porous Ni behaves like an absorptive or emissive effective medium. However, as porosity increases even further, $\bar{\varepsilon}$ decreases to 0.03 since the amount of absorbing metal nanoparticles in the effective medium decreases, so the medium becomes less absorptive as a whole and more transparent. Because there is infrared reflective bulk Ni underneath, the reflectance increases again and thermal emittance decreases. Finally, the solar thermal conversion efficiency η_s in Figure 2e shows that the optimal porosity $\phi \sim 0.5$ and porous height $h \approx 100\text{--}200$ nm can achieve $\eta_s \approx 0.85$.

The simulation results provide a guidance to tune the properties of the Ni porous SSA for solar thermal applications. The thickness and porosity can be controlled by deposited Zn thickness and parameters in the dealloying process (e.g., electrodeposition time and temperature in the vapor-phase dealloying), leading to different porosity ϕ and porous height h . Figure 3 summarizes the experimental results for these two dealloying processes for different electrodeposition times and various heating temperatures. The results show that a longer deposition time results in a lower reflectance at the wider broad band. In the chemical etching dealloying process ($T = 200$ °C), when the deposition time changes from 10 to 30 s, the deposition height of the Zn layer increases from 95 to 285 nm and the nominal porosity increases from 0.12 to 0.42 in Figure 3a (see the Experimental Section for calculation of porosity). The larger porosity and thicker porous layer cause the decrease in reflectance and broader absorptance. Correspondingly, the solar absorptance $\bar{\alpha}$ increases from 0.68 to 0.90 while the thermal emittance $\bar{\varepsilon}$ also increases from 0.07 to 0.22 in Figure 3b,c, which also agrees with the simulation results in Figure 2c,d. On the other hand, for the vapor-phase

dealloying process, with increasing the deposition time from 10 to 120 s, the deposition height of Zn layer increases from 95 to 1139 nm and the porosity increases from 0.12 to 0.42 in Figure 3d. The spectra results show that porous Ni SSAs manifest as a near constant $\bar{\varepsilon}$ (~ 0.1) while a large increase in $\bar{\alpha}$ (0.67 to 0.85) in Figure 3e,f.

These results can be attributed to the different morphologies of Ni particles on the surface of Ni foil in Figures S3 and S4. At the same deposition time, it can be seen that the holes obtained through the chemical etching method are larger and deeper than those of the vapor-phase dealloying method. Therefore, the samples based on the chemical etching method have broader and stronger absorptance in Figure S5a, resulting in the higher solar absorptance and thermal emittance. It also indicates that the Zn layer has not been remarkably alloyed with Ni in the heating process of the vapor-phase dealloying method. Therefore, a long heating process was applied in Figure S5b, whereby a slow heating rate (i.e., long heating time) broadens the absorption region while maintains the thermal emittance unvaried as discussed in the vapor-phase dealloying process at different temperatures. Finally, the absorptance $\bar{\alpha}$ increases from 0.85 to 0.88, and the thermal emittance $\bar{\varepsilon}$ drops from 0.11 to 0.08.

On the basis of the discussions above, it can be found that the dealloying technique is a practical method to achieve highly selective absorption. The selectivity is also tunable to fit different working temperatures and solar intensities. For the vapor-phase dealloying process, the samples usually have low thermal emittance, which is good for high temperature solar selective absorber. On the other hand, for the chemical etching dealloying process, the thermal emittance is slightly higher together with higher solar absorption. Therefore, it is more attractive for low operating temperature since the thermal radiation loss at lower temperature is smaller compared to the solar intensity.

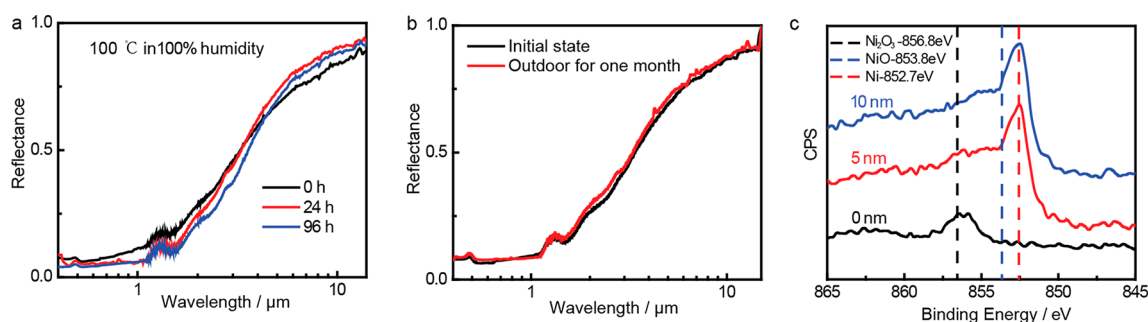


Figure 4. Stability test of the Ni SSAs. (a) Reflectance spectra of Ni porous SSA before heating, after 24 and 96 h heating at 100 °C in 100% humidity. (b) Reflectance spectra of Ni porous SSA before and after being placed in the outdoor environment for one month. (c) Auger spectra of the heat-treated Ni porous SSA taken at the surface as well as ~5 and 10 nm depth below the surface. The black, blue, and red dotted lines in (c) represent the binding energy Ni 2p_{3/2} at the chemical state of Ni₂O₃, NiO, and Ni, which are 856.8, 853.8, and 852.7 eV, respectively.

Table 1. Solar Absorptances $\bar{\alpha}$, Thermal Emittances $\bar{\epsilon}$, and Solar Thermal Efficiency η_s of Ni Absorbers before and after Thermal Stability Tests

time (h)	100 °C in air			100 °C in 100% humidity			200 °C in air			outdoor test for a month			
	$\bar{\alpha}$	$\bar{\epsilon}$	η_s	$\bar{\alpha}$	$\bar{\epsilon}$	η_s	$\bar{\alpha}$	$\bar{\epsilon}$	η_s	$\bar{\alpha}$	$\bar{\epsilon}$	η_s	
0	0.88	0.16	0.70	0.90	0.17	0.71	0.90	0.18	0.69	before	0.90	0.15	0.74
24	0.89	0.15	0.73	0.93	0.12	0.80	0.91	0.16	0.73	after	0.89	0.14	0.74
96	0.90	0.15	0.74	0.94	0.14	0.78	0.92	0.15	0.76				

In real applications, high durability and stability under the operating conditions are required. Therefore, thermal aging tests were conducted at the operation temperature of 100 °C in air or 100% humidity environment for up to 96 h. In addition, thermal aging tests were also performed at higher temperature of 200 °C in air. As shown in Figure 4a,b and Table 1, in all thermal aging tests, the solar absorptance $\bar{\alpha}$ increases while the thermal emittance $\bar{\epsilon}$ decreases with the time evolving. For example, under 100 °C and 100% humidity, $\bar{\alpha}/\bar{\epsilon}$ changes from 0.90/0.17 to 0.94/0.14 after heating for 96 h. Meanwhile, the solar thermal efficiency η_s increases from 0.71 to 0.78. Similarly, after annealing at 100 and 200 °C in air for 96 h, η_s increases from 0.70 to 0.74 and 0.69 to 0.76, respectively. Such improvement is probably attributed to the oxidation of the Ni particles in the thermal aging process, where Ni₂O₃ and NiO are observed on the Ni surface (Figure 4c). Fortunately, NiO_x is well-known to be stable which can protect Ni from further oxidation and retain SSA's optical performance.

To further confirm the durability of the Ni porous SSA, samples were placed outdoors, subject to weather conditions, for a month (see the Experimental Section for details). The results show that the spectral reflectance changes little after a month ($\Delta\bar{\alpha} = -0.006$, $\Delta\bar{\epsilon} = -0.0122$), indicating that such porous Ni SSA has a promising long-term durability (Figure 4b and Table 1). In addition, to examine whether high-temperature operation will cause Ni self-migration and degrade the nanostructure, we calculate Ni self-diffusion at elevated temperatures. At 450 and 500 °C, Ni will only diffuse ~4 and 16 nm in 20 years, respectively, which is much smaller than feature size in our nanostructures (see section S4 of the Supporting Information for more details). The stability of our absorber at higher temperature (e.g., 700 °C) needs to be further studied. Such high temperature (e.g., 700 °C) is attractive for enhancing solar–thermal–electrical efficiency.³³ Currently we consider our approach more suitable for low–medium temperature selective solar absorber applications.^{34,35}

3. CONCLUSIONS

In summary, a scalable dealloying method is demonstrated to fabricate selective solar absorber based on the porous Ni structures. The measured solar absorptance and thermal emittance demonstrate attractive spectral selection with an applicable $\bar{\alpha}/\bar{\epsilon}$ (0.93/0.12 or 0.88/0.08) without the aid of antireflection coating. The thermal stability tests indicate that the porous Ni absorbers are stable at 200 °C in air and 100 °C in a dry and 100% humid environment. Long-term outdoor stability tests also show that the Ni absorbers have excellent durability. The coupled attractive spectral selectivity and high durability make the Ni absorber a promising for use as SSAs. Furthermore, the dealloying technique shows great tunable performance for the selective absorption of metal absorber, which can be widely used to fabricate the porous structures for different working conditions.

4. EXPERIMENTAL SECTION

Reagents. All of the chemicals used in the experiment were of analytical grade, and Ni foils (~0.2 mm thickness) were purchased from China Qingyuan Metal Material Co. Zn was electrodeposited onto the surface of the cathode (i.e., Ni foil) from a Zn plating solution, with a composition of 60 g/L ZnCl₂, 200 g/L KCl, 25 g/L H₃BO₃, and 20 mL/L PEG. All the electrochemical experiments were performed at room temperature with the Pt wire as counter electrode and Ni foils as working electrode. Voltammetry measurements were conducted by using a Biologic VMP3 electrochemical workstation.

Preparation of Porous Ni Absorbers. The Ni foil was sonicated in 12% hydrochloric acid for 2 min to remove the oxide layer and then washed by ethanol and water. After blow-drying, one side of the Ni foil was covered by insulation tape and the other side exposed for further electrodeposition. During the Zn electrodeposition process, constant current was applied to the working electrode, which served as cathode, and the current density was maintained at 20 mA cm⁻². The thickness of Zn film in the experiments can be controlled by altering the duration of the electrodeposition process. After electrodeposition, the metal foil was rinsed by deionized water and dried at room temperature. Then, the sample was heated at different temperatures with different heating rate under the protection of N₂ gas. Finally, two dealloying steps were conducted to remove the Zn

component. When the temperature was below 200 °C, only Zn–Ni alloy formed in the heating process, and then the Zn was removed by the chemical etching dealloying process using the 5 wt % NaOH solution. On the other hand, when the heating temperature was above 300 °C, the Zn component was removed by the vapor-phase dealloying process directly. Finally, the sample was washed by water and blow-drying.

Simulation. Numerical full-field electromagnetic simulations were performed based on the finite-element method (FEM) using the commercial software package COMSOL Multiphysics. To simplify the simulation, periodic boundary conditions are used for the unit cell of the sample. A plane wave is excited from the port on the side of the unit cell with a power of 1 W. The reflection (R), transmission (T), and absorption (A) are calculated by $R = |S_{11}|^2$, $T = |S_{21}|^2$, and $A = 1 - R - T$, respectively, where S_{11} and S_{21} are the scatter parameters. The optical constant of Ni used in the simulation is obtained from Rakic's study.³⁶

Reflectance Measurement. The reflectance of the porous Ni SSAs was measured based on the integrating sphere. For the visible to near-infrared region (0.41–1.05 μm), the reflectance was measured by a continuum laser (SuperK Extreme, NKT Photonics), a tunable filter (Fianium LLTF contrast), and an integrating sphere (Model IS200, Thorlabs). For near-infrared to mid-infrared (1.06–14 μm), a Fourier transform infrared (FT-IR) spectrometer (Vertex 70v, Bruker) coupled with a gold integrating sphere (Model 4P-GPS-020-SL, Labsphere) was used to measure the reflectance. In all measurements, gold-coated aluminum foils were used as the reference to calibration measured results.

Material Characterizations. Auger electron spectroscopy was performed on one thermally annealed Ni porous SSA. The spectra for different depths from the surfaces were obtained by etching with an argon ion beam. A Zeiss Sigma VP scanning electron microscope was used to characterize the nanoporous structure of Ni absorber. For porous Ni SSAs synthesized under different parameters, the surface porosity in the layers imaged from the top was measured using software ImageJ.

Thermal Stability Tests. Thermal aging tests were conducted at the operation temperature of 100 °C in air or 100% humidity environment for up to 96 h. In addition, thermal aging tests were also performed at higher temperature of 200 °C in air. The spectral reflectance of samples was measured before the heating process, and then the reflectance was recorded after heating 24 and 96 h. After heating in air for 96 h at 100 °C, Ni SSAs were placed outdoor in the natural environment without any coating for 1 month (May 2018 at New York City) to investigate its long-term durability. The spectral reflectance of the samples was measured prior to and after the test.

■ ASSOCIATED CONTENT

● Supporting Information

The Supporting Information is available free of charge on the ACS Publications website at DOI: 10.1021/acsam.9b01112.

Ni absorber preparation by dealloying; simulation of the porous Ni SSA; characterization of the porous Ni SSA; self-diffusion calculation of the porous Ni SSA (PDF)

■ AUTHOR INFORMATION

Corresponding Author

*E-mail: yy2664@columbia.edu (Y.Y.).

ORCID

Meijie Chen: 0000-0001-5742-4160

Qian Cheng: 0000-0001-5510-2977

Yurong He: 0000-0003-3009-0468

Yuan Yang: 0000-0003-0264-2640

Notes

The authors declare no competing financial interest.

■ ACKNOWLEDGMENTS

Y.Y. acknowledges support from Columbia University. M.C. acknowledges funding support from the China Scholarship Council (CSC) graduate scholarship.

■ REFERENCES

- (1) Burschka, J.; Pellet, N.; Moon, S. J.; Humphry-Baker, R.; Gao, P.; Nazeeruddin, M. K.; Grätzel, M. Sequential Deposition as a Route to High-Performance Perovskite-Sensitized Solar Cells. *Nature* **2013**, *499* (7458), 316–319.
- (2) Balzani, V.; Credi, A.; Venturi, M. Photochemical Conversion of Solar Energy. *ChemSusChem* **2008**, *1* (1–2), 26–58.
- (3) Ren, H.; Tang, M.; Guan, B.; Wang, K.; Yang, J.; Wang, F.; Wang, M.; Shan, J.; Chen, Z.; Wei, D.; Peng, H.; Liu, Z. Hierarchical Graphene Foam for Efficient Omnidirectional Solar–Thermal Energy Conversion. *Adv. Mater.* **2017**, *29* (38), 1702590.
- (4) Kraemer, D.; Poudel, B.; Feng, H. P.; Caylor, J. C.; Yu, B.; Yan, X.; Ma, Y.; Wang, X.; Wang, D.; Muto, A.; McEnaney, K.; Chiesa, M.; Ren, Z.; Chen, G. High-Performance Flat-Panel Solar Thermoelectric Generators with High Thermal Concentration. *Nat. Mater.* **2011**, *10* (7), 532–538.
- (5) Lewis, N. S. Research Opportunities to Advance Solar Energy Utilization. *Science* **2016**, *351* (6271), aad1920.
- (6) Mandal, J.; Wang, D.; Overvig, A. C.; Shi, N. N.; Paley, D.; Zangiabadi, A.; Cheng, Q.; Barmak, K.; Yu, N.; Yang, Y. Scalable, “Dip-and-Dry” Fabrication of a Wide-Angle Plasmonic Selective Absorber for High-Efficiency Solar–Thermal Energy Conversion. *Adv. Mater.* **2017**, *29* (41), 1702156.
- (7) Mandal, J.; Fu, Y.; Overvig, A. C.; Jia, M.; Sun, K.; Shi, N. N.; Zhou, H.; Xiao, X.; Yu, N.; Yang, Y. Hierarchically Porous Polymer Coatings for Highly Efficient Passive Daytime Radiative Cooling. *Science* **2018**, *362* (6412), 315–319.
- (8) Mandal, J.; Du, S.; Dontigny, M.; Zaghbi, K.; Yu, N.; Yang, Y. $\text{Li}_4\text{Ti}_5\text{O}_{12}$: A Visible-to-Infrared Broadband Electrochromic Material for Optical and Thermal Management. *Adv. Funct. Mater.* **2018**, *28* (36), 1802180.
- (9) Duffie, J. A.; Beckman, W. A. *Solar Engineering of Thermal Processes*, 4th ed.; Wiley: 2013.
- (10) Li, X.; Ni, G.; Cooper, T.; Xu, N.; Li, J.; Zhou, L.; Hu, X.; Zhu, B.; Yao, P.; Zhu, J. Measuring Conversion Efficiency of Solar Vapor Generation. *Joule* **2019**, 1–5.
- (11) Kennedy, C. E. *Review of Mid- to High-Temperature Solar Selective Absorber Materials*; National Renewable Energy Lab.: Golden, CO, 2002.
- (12) Tesfamichael, T.; Wäckelgård, E. Angular Solar Absorptance and Incident Angle Modifier of Selective Absorbers for Solar Thermal Collectors. *Sol. Energy* **2000**, *68* (4), 335–341.
- (13) Bermel, P.; Lee, J.; Joannopoulos, J. D.; Celanovic, I.; Soljacic, M. Selective Solar Absorbers. *Annu. Rev. Heat Transfer* **2012**, *15* (15), 231–254.
- (14) Tesfamichael, T.; Roos, A. Treatment of Antireflection on Tin Oxide Coated Anodized Aluminum Selective Absorber Surface. *Sol. Energy Mater. Sol. Cells* **1998**, *54* (1–4), 213–221.
- (15) Wang, H.; Wang, L. Perfect Selective Metamaterial Solar Absorbers. *Opt. Express* **2013**, *21* (S6), A1078.
- (16) Selvakumar, N.; Krupanidhi, S. B.; Barshilia, H. C. Carbon Nanotube-Based Tandem Absorber with Tunable Spectral Selectivity: Transition from near-Perfect Blackbody Absorber to Solar Selective Absorber. *Adv. Mater.* **2014**, *26* (16), 2552–2557.
- (17) Chen, M.; He, Y. Plasmonic Nanostructures for Broadband Solar Absorption Based on the Intrinsic Absorption of Metals. *Sol. Energy Mater. Sol. Cells* **2018**, *188*, 156–163.
- (18) Zhou, L.; Zhuang, S.; He, C.; Tan, Y.; Wang, Z.; Zhu, J. Self-Assembled Spectrum Selective Plasmonic Absorbers with Tunable Bandwidth for Solar Energy Conversion. *Nano Energy* **2017**, *32*, 195–200.
- (19) Lu, J. Y.; Raza, A.; Noorulla, S.; Alketbi, A. S.; Fang, N. X.; Chen, G.; Zhang, T. J. Near-Perfect Ultrathin Nanocomposite

Absorber with Self-Formed Topping Plasmonic Nanoparticles. *Adv. Opt. Mater.* **2017**, *5* (18), 1700222.

(20) Cuomo, J. J.; Ziegler, J. F.; Woodall, J. M. A New Concept for Solar Energy Thermal Conversion. *Appl. Phys. Lett.* **1975**, *26* (10), 557–559.

(21) Sai, H.; Yugami, H.; Kanamori, Y.; Hane, K. Solar Selective Absorbers Based on Two-Dimensional W Surface Gratings with Submicron Periods for High-Temperature Photothermal Conversion. *Sol. Energy Mater. Sol. Cells* **2003**, *79* (1), 35–49.

(22) Yeng, Y. X.; Ghebrehbrhan, M.; Bermel, P.; Chan, W. R.; Joannopoulos, J. D.; Soljacic, M.; Celanovic, I. Enabling High-Temperature Nanophotonics for Energy Applications. *Proc. Natl. Acad. Sci. U. S. A.* **2012**, *109* (7), 2280–2285.

(23) Rinnerbauer, V.; Ndao, S.; Xiang Yeng, Y.; Senkevich, J. J.; Jensen, K. F.; Joannopoulos, J. D.; Soljačić, M.; Celanovic, I.; Geil, R. D. Large-Area Fabrication of High Aspect Ratio Tantalum Photonic Crystals for High-Temperature Selective Emitters. *J. Vac. Sci. Technol., B: Nanotechnol. Microelectron.: Mater., Process., Meas., Phenom.* **2013**, *31* (1), 011802.

(24) Beermann, J.; Eriksen, R. L.; Søndergaard, T.; Holmgaard, T.; Pedersen, K.; Bozhevolnyi, S. I. Plasmonic Black Metals by Broadband Light Absorption in Ultra-Sharp Convex Grooves. *New J. Phys.* **2013**, *15* (7), 073007.

(25) Craighead, H. G.; Howard, R. E.; Tennant, D. M. Textured Thin-Film Si Solar Selective Absorbers Using Reactive Ion Etching. *Appl. Phys. Lett.* **1980**, *37* (7), 653–655.

(26) Selvakumar, N.; Barshilia, H. C. Review of Physical Vapor Deposited (PVD) Spectrally Selective Coatings for Mid- and High-Temperature Solar Thermal Applications. *Sol. Energy Mater. Sol. Cells* **2012**, *98*, 1–23.

(27) Selvakumar, N.; Barshilia, H. C.; Rajam, K. S.; Biswas, A. Structure, Optical Properties and Thermal Stability of Pulsed Sputter Deposited High Temperature HfO_x/Mo/HfO₂ solar Selective Absorbers. *Sol. Energy Mater. Sol. Cells* **2010**, *94* (8), 1412–1420.

(28) Li, P.; Liu, B.; Ni, Y.; Liew, K. K.; Sze, J.; Chen, S.; Shen, S. Large-Scale Nanophotonic Solar Selective Absorbers for High-Efficiency Solar Thermal Energy Conversion. *Adv. Mater.* **2015**, *27* (31), 4585–4591.

(29) Boström, T.; Wäckelgård, E.; Westin, G. Solution-Chemical Derived Nickel-Alumina Coatings for Thermal Solar Absorbers. *Sol. Energy* **2003**, *74* (6), 497–503.

(30) Li, Z.; Zhao, J.; Ren, L. Aqueous Solution-Chemical Derived Ni-Al₂O₃ Solar Selective Absorbing Coatings. *Sol. Energy Mater. Sol. Cells* **2012**, *105*, 90–95.

(31) Wazwaz, A.; Salmi, J.; Hallak, H.; Bes, R. Solar Thermal Performance of a Nickel-Pigmented Aluminium Oxide Selective Absorber. *Renewable Energy* **2002**, *27* (2), 277–292.

(32) Lu, Z.; Li, C.; Han, J.; Zhang, F.; Liu, P.; Wang, H.; Wang, Z.; Cheng, C.; Chen, L.; Hirata, A.; Fujita, T.; Erlebacher, J.; Chen, M. Three-Dimensional Bicontinuous Nanoporous Materials by Vapor Phase Dealloying. *Nat. Commun.* **2018**, *9* (1), 276.

(33) Cao, F.; Tang, L.; Li, Y.; Litvinchuk, A. P.; Bao, J.; Ren, Z. A High-Temperature Stable Spectrally-Selective Solar Absorber Based on Cermet of Titanium Nitride in SiO₂ Deposited on Lanthanum Aluminate. *Sol. Energy Mater. Sol. Cells* **2017**, *160*, 12–17.

(34) Yang, Y.; Yan, Q.; Zhai, R.; Kouzani, A.; Hu, E. An Efficient Way to Use Medium-or-Low Temperature Solar Heat for Power Generation - Integration into Conventional Power Plant. *Appl. Therm. Eng.* **2011**, *31* (2–3), 157–162.

(35) Delgado-Torres, A. M.; García-Rodríguez, L. Analysis and Optimization of the Low-Temperature Solar Organic Rankine Cycle (ORC). *Energy Convers. Manage.* **2010**, *51* (12), 2846–2856.

(36) Rakić, A. D.; Djurišić, A. B.; Elazar, J. M.; Majewski, M. L. Optical Properties of Metallic Films for Vertical-Cavity Optoelectronic Devices. *Appl. Opt.* **1998**, *37* (22), 5271.